Superconductivity in La₂Ni₂In

Jannis Maiwald,[1,2,*] Igor I. Mazin,[3,4] Alex Gurevich,[5] and Meigan Aronson[1,2]

[1]*Quantum Matter Institute, University of British Columbia, Vancouver, BC, Canada V6T 1Z4*
[2]*Department of Physics and Astronomy, University of British Columbia, Vancouver, BC, Canada V6T 1Z1*
[3]*Department of Physics and Astronomy, George Mason University, Fairfax, Virginia 22030, USA*
[4]*Quantum Science and Engineering Center, George Mason University, Fairfax, Virginia 22030, USA*
[5]*Department of Physics, Old Dominion University, Norfolk, Virginia 23529, USA*

We report here the properties of single crystals of La₂Ni₂In. Electrical resistivity and specific heat measurements concur with the results of density functional theory calculations, finding that La₂Ni₂In is a weakly correlated metal, where the Ni magnetism is almost completely quenched, leaving only a weak Stoner enhancement of the density of states. Superconductivity is observed at temperatures below 0.9 K. A detailed analysis of the field and temperature dependencies of the resistivity, magnetic susceptibility, and specific heat at the lowest temperatures reveals that La₂Ni₂In is a dirty type-II superconductor with likely s-wave gap symmetry. Nanoclusters of ferromagnetic inclusions significantly affect the subgap states resulting in a nonexponential temperature dependence of the specific heat $C(T)$ at $T \ll T_c$.

I. INTRODUCTION

Electronic correlations lead to an array of different ordered and disordered phases in metals. These phases are especially interesting when they occur on low-dimensional or geometrically frustrated lattices. If the correlations are not strong enough to render the system fully insulating, the stabilization of increasingly localized electronic states and the associated magnetic moments adds a compelling complexity to the phase behaviors of correlated metals. Finding isostructural, and even isoelectronic, systems where the relationships between the different phases and behaviors can be explored in a controlled way is of great importance. The R_2T_2X (R = rare earth, T = transition metal, X = main group, pnictogen, chalcogen) family has proven particularly useful, due to its unique crystal structure [1–3]. The lattice of f-electron bearing rare-earth atoms R consists of planes of orthogonal dimers, as in the Shastry-Sutherland lattice (SSL), that are stacked along the c axis. Depending on the relative distances between the rare-earth moments in the plane or perpendicular to the plane, two-dimensional systems of isolated SSL planes [4,5] can be realized, or alternatively spin ladder systems [6,7]. For R_2T_2X (R = Ce,Yb), the f electrons of the rare earths can also display mixed valence behaviors [8–13], indicating that coupling of the f electrons to extended states can lead to the overall suppression of magnetic moments. It is expected that the interplay of strong quantum fluctuations due to the unique R_2T_2X lattice [13–15], as well as proximity to the delocalization of the f electrons via the Kondo effect, can result in the destabilization of ordered phases, and to the formation of quantum critical points (QCPs) where the host systems are transitioning among

different phases [9,13,16–18]. Given this richness of behavior when the rare earth R has f electrons, it is surprising that relatively little is known about compounds from this family where R = La,Lu,Y, where there are no valence f electrons. Here, there is the possibility of instead studying d-electron magnetism and correlations that are associated with the T atoms. At present, 21 compounds have been identified where R = Y,La,Lu, T = Ni,Cu,Au,Pt,Pd,Rh, and X = Mg,In,Pb,Cd. However, there has been relatively little study of the physical properties of these compounds [11], and to our knowledge none of these studies have been carried out on single crystals.

Of the known R_2T_2X compounds with R = Y,La,Lu, it seems likely that compositions with T = Ni have magnetic character. For that reason, we focused initially on La₂Ni₂In. Previous measurements were carried out on polycrystalline samples [11], where the possibility of small inclusions of multiple phases, and the lack of a well-defined conduction path could potentially complicate interpretation. We report here a detailed study of the basic properties of La₂Ni₂In crystals. Electrical resistivity measurements find that this compound is metallic. Density functional theory (DFT) calculations of the electronic structure reveal that there is considerable charge transfer associated with the Ni d states, which are well below the Fermi level. Thus, the manifestations of the d-electron character are very weak. Specific heat measurements concur that the mass enhancement of the quasiparticles is quite small, in good agreement with the DFT calculations. Measurements of the magnetic susceptibility confirm the weak magnetism predicted by the DFT calculations, revealing that there are no localized magnetic moments, and the only intrinsic part of the magnetic susceptibility is the temperature-independent Pauli susceptibility with a minimal Stoner enhancement. Overall, La₂Ni₂In is a weakly correlated metal, with minimal magnetic character. We find that it undergoes a transition to a

*jannis.maiwald@ubc.ca

superconducting state below 0.89 K. A detailed analysis of the specific heat, electrical resistivity, and magnetic susceptibility in the superconducting state was carried out, revealing that La_2Ni_2In is a conventional type-II superconductor in the dirty limit.

II. METHODS

Single crystals of La_2Ni_2In were synthesized using a LaNi self-flux. The precursor LaNi was prepared using a solid-state reaction. Stoichiometric amounts of La (99.9%) and Ni (99.995%) were cut into small pieces and placed into an Al_2O_3 crucible, sealed under $\sim$250 mbar argon atmosphere in a quartz tube and successively heated to about $1100\,°C$ for 40 h. The above steps were carried out under a protective argon atmosphere to prevent lanthanum from oxidizing. After synthesis the precursor was ground into a powder.

The precursor and elemental In (99.999%) were mixed in a ratio of 6:1 and placed in a Canfield crucible set (two Al_2O_3 crucibles separated by a strainer) and then sealed as described above. The sealed quartz tubes were heated in an open furnace over the course of 3 h to $770\,°C$, where they remained for 5 h to ensure adequate mixing of the reactants. Growth of La_2Ni_2In single crystals took place while lowering the temperature over a period of 15 h down to $725\,°C$. At this temperature the still liquid self-flux was separated from the crystals by placing the batch upside down in a centrifuge and spinning it at 2000–3000 rpm for about 15 s. Using this procedure we were able to grow needlelike single crystals of La_2Ni_2In. Typical dimensions of the crystals are about $0.5 \times 0.5 \times 4$ mm^3. An image of the five single crystals used for heat capacity measurements is shown in Fig. 1(a).

Powder x-ray diffraction (XRD) patterns were recorded with a Bruker D8 Focus diffractometer in the Bragg-Bretano configuration using a Co cathode. The program FULLPROF was used to refine the powder diffraction patterns. Measurements of the electrical resistivity and specific heat were obtained using a Physical Property Measurement System from Quantum Design equipped with a He^3/He^4 dilution refrigerator insert. Measurements of the magnetic susceptibility were done using a Magnetic Property Measurement System 3 also from Quantum Design and equipped with a He^3 insert.

Band structure calculations were performed using the linear augmented plane wave code WIEN2K [19]. For the calculations of the zone-center phonons the VASP pseudopotential package was used [20]. The gradient-corrected density functional of Ref. [21] was used in all calculations.

III. NORMAL STATE PROPERTIES

A. Sample characterization

The as-grown single crystals of La_2Ni_2In were structurally characterized by powder x-ray diffraction. The diffraction pattern and its refinement are compared in Fig. 1. All recorded diffraction peaks can be indexed within the reported tetragonal structure [3], which has the space group $P4/mbm$. The absence of extrinsic diffraction peaks rules out crystalline impurity phases with concentrations larger than $\simeq 1$ %. The refined lattice parameters and atomic coordinates are presented in Table I. In particular, the refined a and c lattice constants for
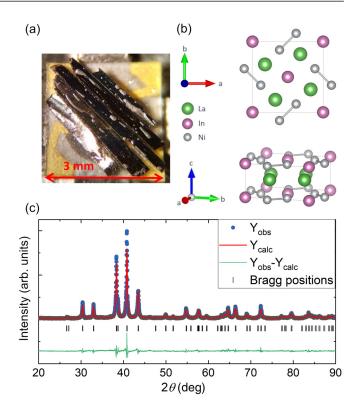

FIG. 1. (a) Optical microscope image of five single crystals of La_2Ni_2In. (b) The refined crystal structure of La_2Ni_2In. The unit cell (thin gray lines) is shown in (top) top view and (bottom) perspective view. Gray solid lines depict the nearest-neighbor Ni distance of 0.253 nm. (c) Measured powder XRD pattern of as-grown La_2Ni_2In, and its refinement using the reported tetragonal structure with space group $P4/mbm$. Bragg peak positions are indicated.

our single crystals lie within the range of values reported for annealed polycrystalline samples [11,22]. This indicates that the presence of defects and/or nonstoichiometry in the latter is rather limited. We attribute the minor differences between the observed and refined intensities in the XRD pattern to possible vacancies and/or site exchange, which are not uncommon in polycrystalline R_2T_2X compounds [23]. Finally, we found no indication of a phase with an orthorhombic structure, as reported earlier [23]. In fact, forcing the orthorhombic structure for the Rietveld refinement requires additional peaks that are not observed in our measured data. A comparison between the tetragonal and orthorhombic refinements can be found in Appendix A.

Like most of the R_2T_2X compounds, La_2Ni_2In adopts the tetragonal Mo_2FeB_2-type structure with space group

TABLE I. Results of the XRD Rietvelt refinement.

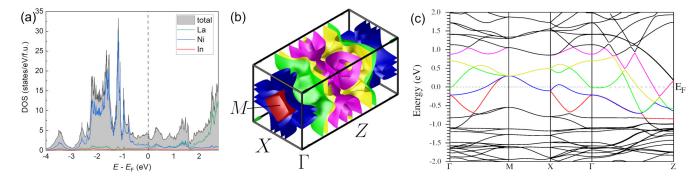| Lattice parameters	a (nm)	c (nm)	c/a
Single crystal	0.76448(2)	0.389149(14)	0.5009
Atomic coordinates	x	y	z
La ($4h$)	0.17708	0.67708	0.5
Ni ($4g$)	0.61708	0.11708	0.0
In ($2a$)	0.0	0.0	0.0

FIG. 2. Density functional calculation results for La$_2$Ni$_2$In. (a) Density of states as a function of energy E relative to the Fermi energy E_F. (b) Fermi surface calculated using the tetragonal crystal structure determined from our XRD analysis. The colors refer to Fermi level crossings of bands with the same colors (c). (c) Electronic band structure plotted along high-symmetry directions.

$P4/mbm$, which is an ordered derivative of the U$_3$Si$_2$ structure where the X atom occupies one of the two inequivalent U sites. Figure 1(b) shows that, like the R atoms, the Ni atoms form dimers with the closest Ni-Ni distance (solid gray bonds) of 0.253 nm. The dimers form a square lattice in the a-b plane, where the closest interdimer distance is 0.541 nm. The Ni-Ni distance along the c axis is 0.389 nm, indicating a quasi-two-dimensional environment for the Ni subsystem.

B. Density functional calculations of the electronic structure

We have performed *ab initio* band structure calculations using the experimentally determined tetragonal structure of La$_2$Ni$_2$In. The calculated density of states (DOS) and Fermi surface of La$_2$Ni$_2$In are depicted in Fig. 2. In view of the above-mentioned proposal of an orthorhombic structural variant [23], we have as well attempted a full structural optimization in both crystallographic groups. The tetragonal $P4/mbm$ structure optimized into $a = 0.7663$ nm and $c = 0.3906$ nm, with the internal parameters, in the order of Table I, being 0.1772, 0.6772, 0.6181, and 0.1181. The orthorhombic $Pbam$ structure optimizes into $a = 0.7643$, $b = 1.5595$, and $c = 0.3903$ nm, with La $4g$ (0.6068, 0.2840, 0) and (0.7438, 0.5361, 0), Ni $4h$ (0.5565, 0.4251, 0.5) and (0.3044, 0.3189, 0.5), and In $4h$ (0.4259, 0.1276, 0.5). Curiously, the latter structure is lower in energy by $\approx$ 30 meV/formula, consistent with the orthorhombic structure found in polycrystalline samples [23], but not in our single-crystal samples, where the tetragonal structure is stabilized. We will use the results from the tetragonal refinement for our analysis of La$_2$Ni$_2$In.

The Ni-based states form a broad band between $\simeq -2$ and -1 eV [Fig. 2(a)]. The breadth of the band reflects a combination of hybridization and charge transfer, indicating that Ni likely has little magnetic character. There is a robust density of states at the Fermi level E_F, confirming that La$_2$Ni$_2$In is metallic. The Ni d states contribute little weight at E_F, and so we conclude that the metal will have at most weak magnetic correlations. Accordingly, we also performed fixed spin moment calculations to determine the Stoner-renormalized spin susceptibility, which appears to be about 33% higher than the Pauli susceptibility. This is a modest Stoner enhancement, typical for nonmagnetic metals such as Al. While Ni is often

magnetic or close to magnetic in many of its compounds, magnetism is almost completely quenched in La$_2$Ni$_2$In.

The Fermi surface of La$_2$Ni$_2$In is depicted in Fig. 2(b). The five sheets of the Fermi surface correspond to band crossings that are evident in the electronic band structure [Fig. 2(c)]. It is notable that two of these sheets show little dispersion along Γ-M, possibly suggesting a weak two-dimensionality that is not inconsistent with the layered character of the La$_2$Ni$_2$In crystal structure (Fig. 1). The calculated plasma frequencies along the crystallographic a and c directions are 3.31 and 3.98 eV, corresponding to the Fermi velocities of 0.19×10^8 and 0.23×10^8 cm/s, respectively. In addition, we calculated the frequencies of the zone-center phonons, which can be found in Appendix B.

C. Specific heat

The temperature dependence of the specific heat $C(T)$ of La$_2$Ni$_2$In is presented in Fig. 3. C rises monotonically with increasing temperatures T between 0.05 and 300 K, reaching the Dulong-Petit value of $3nR$ with $n = 5$ atoms per formula unit (f.u.) around 300 K. However, our data are not well described by the standard Debye model alone. Since the Debye model only accounts for acoustic modes, this may suggest that low-energy optical modes may be present in La$_2$Ni$_2$In. This expectation was confirmed in our calculations of the zone-center phonon spectrum (see Table III, Appendix B), where a number of low-lying optical modes were found. This motivated us to model the measured specific heat C using a Debye-Einstein model:

$$C = C_e + mC_D + (1 - m)C_E. \tag{1}$$

The weighting factor m enforces the requirement that the acoustic and optical modes must together provide a fixed amount of specific heat $3nR$ at sufficiently large T. The assumption behind the formulation in (1) is that the acoustic modes are described by the Debye term. The single Einstein mode provides an empirical equivalence for the spectrum of optical modes, whose computed values are given in Table III of Appendix B. The electron and phonon contributions to the specific heat are given by $C_e = \gamma T$ and the Debye and
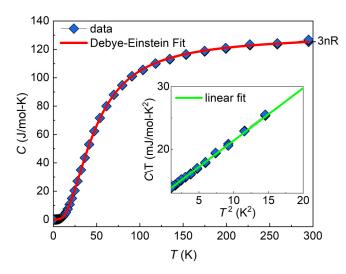
FIG. 3. Specific heat $C(T)$ of La_2Ni_2In as a function of temperature T between 0.05 and 300 K. The red line is a fit to the data using the model defined in the main text. $3nR$ denotes the Dulong-Petit constant with $n = 5$. Inset: Specific heat C/T as a function of T^2 between 1 and 4.5 K. The solid green line is a fit to the expression $C(T) = \gamma T + \beta T^3$, yielding a Sommerfeld coefficient of $\gamma = 13.01(3)$ mJ mol^{-1} K^{-2}.

Einstein terms

$$C_D = 9nN_A k_B \left(\frac{T}{T_D}\right)^3 \int_0^{T_D/T} \frac{x^4}{(e^x - 1)(1 - e^{-x})} dx,$$

$$C_E = 3nN_A k_B \left(\frac{T_E}{T}\right)^2 \frac{1}{(e^{T_E/T} - 1)(1 - e^{-T_E/T})},$$

respectively, with the Sommerfeld coefficient γ, Avogadro's constant N_A, Boltzmann's constant k_B, and T_E the Einstein temperature. The data are well described with the following parameters: $\gamma = 11.3(3)$ mJ mol^{-1} K^{-2}, $T_D = 211 \pm 1$ K, $T_E = 85 \pm 1$ K, and $m = 0.82(1)$.

We also extracted γ and T_D from a linear fit to C/T as a function of T^2 at low temperatures between 1 and 4 K (see inset of Fig. 3) using the expression $C(T) = \gamma T + \beta T^3$, with $\beta = 12\pi^4/5nN_A k_B/T_D^3$. This procedure resulted in $\gamma = 13.01(3)$ mJ mol^{-1} K^{-2} and $T_D = 226 \pm 1$ K, which are in reasonable agreement with the values found in the more comprehensive fit above. In the following we will use the values obtained from the low-temperature fit. The derived Sommerfeld coefficient corresponds to 5.52(3) states/eV/f.u. at the Fermi level, which is 38% larger than the value from our DFT calculations (≈ 4.0 states/eV/f.u.). Given the apparent absence of magnetic correlations in the DFT calculations, we conclude that this mass renormalization is a consequence of electron-phonon coupling, with a magnitude $\lambda_{m^*/m} = 0.38$.

D. Electrical resistivity

Figure 4 shows the electrical resistivity $\rho(T)$ of La_2Ni_2In as a function of temperature T in the range of 0.15–400 K. The measuring current was applied along the crystallographic c axis. The room-temperature value $\rho_{300 \text{ K}} = 63\,\mu\Omega\text{cm}$

TABLE II. Normal and superconducting properties of La_2Ni_2In. The abbreviations "calc" and "expt." attached to some of the variables distinguishes theoretical from experimental results.

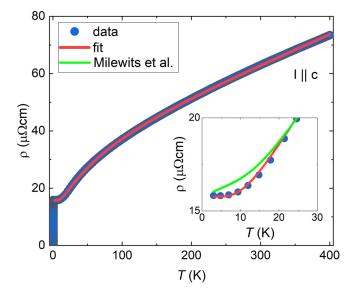| Parameter	Unit	Value
T_c	K	0.89
$H_{c2}(0)$	Oe	1918
$\xi(0)$	nm	34.4
ξ_0^{calc}	nm	245
$\xi^{\text{calc}}(0)$	nm	42.3
ℓ_{mfp}	nm	10
$H_{c1}(0)/(1-N)$	Oe	14.0
H_{c1}^{calc}	Oe	13.7
λ_L^{calc}	nm	250
$\lambda_{L0}^{\text{calc}}$	nm	50
κ_{GL}		7.3
γ_n	mJ mol^{-1} K^{-2}	13.01
β	mJ mol^{-1} K^{-4}	0.84
T_D	K	226
λ_{MM}		0.461
λ_{tr}		0.395
$\lambda_{m^*/m}$		0.38
ω_p^a	eV	3.31
ω_p^c	eV	3.98
$N(0)$	states/eV/f.u.	3.96
χ_{Pauli}	10^{-4}emu/mol	1.3
χ_{calc}	10^{-4}emu/mol	1.7
$\chi_{\text{expt.}}$	10^{-4}emu/mol	2.1
$\Delta C/\gamma_n T_c$		1.21
$\Delta(0)/k_B T_c$		1.26

FIG. 4. Temperature dependence of the electrical resistivity $\rho(T)$ of La_2Ni_2In, with the measuring current I applied along the crystallographic c axis. The data (blue symbols) are well described by the heuristic model (red line) with an exponential factor as discussed in the main text. Inset: Low-temperature region of $\rho(T)$, showing the difference between our heuritsic fit and the fit to the model reported by Milewits *et al.* [24] using an exponential term (green line).

TABLE III. Calculated phonon energies of La$_2$Ni$_2$In at the center (Γ point) of the Brillouin zone.

No.	Phonon energy			
	THz	2π THz	cm^{-1}	meV
1	4.22229	26.52944	140.8405	17.462
2	4.20341	26.41078	140.2106	17.3839
3	4.00624	25.17197	133.6339	16.5685
4	4.00624	25.17197	133.6339	16.5685
5	3.78668	23.79244	126.3102	15.66047
6	3.54148	22.25177	118.131	14.64638
7	3.54148	22.25177	118.131	14.64638
8	3.52643	22.15721	117.629	14.58414
9	3.28964	20.66944	109.7307	13.60488
10	3.28964	20.66944	109.7307	13.60488
11	3.07298	19.30812	102.5037	12.70884
12	3.06187	19.23831	102.1331	12.66289
13	2.98852	18.7774	99.68617	12.35952
14	2.80868	17.64744	93.68741	11.61576
15	2.80827	17.64488	93.67381	11.61408
16	2.80827	17.64488	93.67381	11.61408
17	2.70542	16.99868	90.24323	11.18874
18	2.70542	16.99868	90.24323	11.18874
19	2.55974	16.08329	85.38359	10.58622
20	2.41802	15.19286	80.65641	10.00012
21	2.34038	14.70504	78.06667	9.67904
22	2.34038	14.70504	78.06667	9.67904
23	2.11171	13.26824	70.43892	8.73332
24	2.10024	13.19619	70.05642	8.68589
25	1.78281	11.20173	59.46814	7.37311
26	1.53756	9.66074	51.2873	6.35882
27	1.53756	9.66074	51.2873	6.35882

identifies La$_2$Ni$_2$In as a good metal, while the residual resistivity ratio (RRR) $\rho_{300\,\mathrm{K}}/\rho_{2\,\mathrm{K}} = 4$ indicates significant defect scattering at low temperatures that is evidenced by the rather large residual resistivity $\rho_0 \simeq 16\,\mu\Omega$cm (inset Fig. 4). Nonetheless, the absolute values of ρ_0 in our single crystals are smaller than those reported in polycrystalline samples by factors of 3–5 [11]. While this may reflect a higher defect concentration in the polycrystalline samples, we have also noticed the formation of a low-conductivity passivated surface layer on our single crystals when they are exposed to air over time. The greater surface area of polycrystalline samples, combined with the uncertain current paths, could plausibly lead to significantly higher resistivity in polycrystalline samples than in freshly prepared single crystals.

The resistivity of single crystals decreases monotonically with decreasing temperature, as expected in a good metal (Fig. 4). The decrease at high temperatures initially has a sublinear slope, leading to an inflection point around 30 K. The resistivity approaches its residual value ρ_0, but below 0.89 K the resistance drops sharply to zero, indicating a transition into a superconducting state. This transition is extremely sharp, having a width $\Delta T_c \approx 80$ mK.

The normal state resistivity $\rho(T)$ in the range 2–30 K is reasonably well described by scattering of weakly correlated quasiparticles from acoustic phonons, as described by the Bloch-Grüneisen law:

$$\rho(T) = \rho_0 + \rho_D(T), \qquad (2)$$

$$\rho_D(T) = A\left(\frac{T}{T_D}\right)^5 \int_0^{T_D/T} \frac{x^5 dx}{(e^x - 1)(1 - e^{-x})}, \qquad (3)$$

where $T_D = 226$ K is the Debye temperature taken from the specific heat analysis. This fit agrees reasonably well with the measured $\rho(T)$ between 0.89 and 30 K, but not above 30 K. Inspired by the analysis of the specific heat, we added an Einstein term, $\rho_E(T) = B(T_E/T)/(e^{T_E/T} - 1)(1 - e^{-T_E/T})$, to the fit. However, this did not lead to any appreciable improvement in the goodness of fit.

Adding an exponential term, $B \exp(-T_0/T)$, that accounts for umklapp processes assisted by a specific phonon with an energy T_0 [24,25], improves the agreement between the fit and the data, but does not make it perfect (see green line in Fig. 4, inset). The Mott-Jones expression [26,27] was also considered, but it did not reproduce the curvature of the experimental data. Curiously, adding an exponential *factor*, as in

$$\rho(T) = [\rho_0 + \rho_D(T)][1 + c \exp(-T_0/T)], \qquad (4)$$

generates an essentially perfect fit to the data (Fig. 4), with the following parameters: $\rho_0 = 15.7(1)\,\mu\Omega$ cm, $T_D = 226$ K (taken from the Debye-Einstein fit to our specific heat data), $A = 36.1(2)\,\mu\Omega$ cm, $c = 1.49(1)$, and $T_0 = 42.4(4)$ K. It is interesting that T_0 is essentially half the value of the Einstein mode temperature $T_E = 85$ K that was determined from the fit to the specific heat.

This fit leads to the linear coefficient $d\rho(T)/dT = 0.10\,\mu\Omega$cm/K at large T. Using the Drude formula for the phonon-limited resistivity, we find for the transport electron-phonon coupling constant [28] $\lambda_{\mathrm{tr}} = (d\rho/dT)\omega_p^2/4.01$, where $(d\rho/dT)$ is the high-temperature resistivity coefficient in units $\mu\Omega$cm/K. Taking the calculated plasma frequency along the c axis $\omega_p = 3.98$ eV, we deduce the $\lambda_{\mathrm{tr}} = 0.395$, in good agreement with the value $\lambda_{m^*/m} = 0.38$ from the DFT calculations.

E. Magnetic susceptibility

Although our DFT calculations indicate that La$_2$Ni$_2$In is not appreciably magnetic, measurements of the magnetic moment as a function of the magnetic field applied along the crystallographic c axis at various temperatures (Fig. 5) reveal nonlinearities at low fields that are suggestive of weak ferromagnetism. Hysteresis is observed in $M(H)$ at low temperatures, with a magnitude that decreases with increasing temperature and the dc magnetic susceptibility $\chi = M/H$ is strongly temperature dependent when measured in low fields, but this temperature dependence weakens appreciably in high fields (see Appendix C, Fig. 10).

The magnetization $M(H)$ isotherms that are presented in Fig. 5 are illuminating about the nature of the ferromagnetism that is observed in La$_2$Ni$_2$In. In the spirit of the Arrott plot [29], $M(H)$ is linear at high fields, and the spontaneous moment M_0 can be estimated by extrapolating to zero field. The temperature dependence of M_0 is plotted in Fig. 6, showing that M_0 decreases slowly from its value of $\sim 2.5 \times 10^{-4}\mu_B$/Ni at 1.8 K to $\sim 0.5 \times 10^{-4}\mu_B$/Ni at 300 K. These data indicate
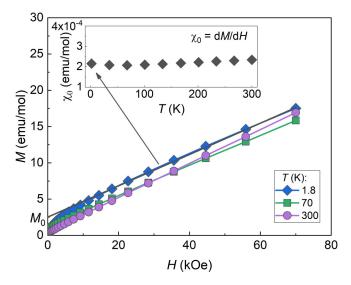
FIG. 5. Magnetization $M(H)$ of La$_2$Ni$_2$In as a function of magnetic field H for various selected temperatures T, as indicated and the effective susceptibility χ_0 (black filled diamonds), determined from $M(H)$ as described in the text. Measurements were carried out on a stack of six coaligned crystals, and the magnetic field is applied parallel to the crystallographic c axis. Extrapolating the high-field data to $H = 0$ (solid black line) gives the indicated intercept M_0, and the slope χ_0.

that the onset of ferromagnetism occurs well above 300 K, and the very slow development of M_0 and the lack of its saturation well below the apparent Curie temperature T_C is inconsistent with the order-parameter behavior observed in
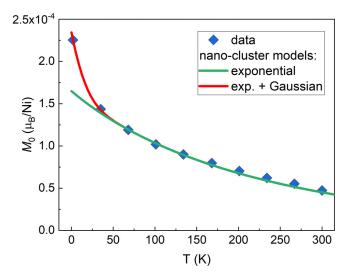

FIG. 6. The temperature dependence of the spontaneous magnetization M_0 (blue diamonds). The data are compared to two models of the ferromagnetic nanoclusters: exponential distribution of cluster sizes (green line) and exponential distribution with additional Gaussian distribution to describe ultrasmall clusters (red line). See Eq. (5) and discussion in the text. Measurements of different samples (Appendix C) find that the distribution of nanocluster sizes does not change appreciably among crystals taken from the same batch, although the total amount of magnetic material does differ moderately.

pristine, bulk ferromagnets. The most likely interpretation of these data is that the ferromagnetism originates with a contaminant phase that was introduced during the synthesis on the surface or as an inclusion in our single crystals. Elemental Ni with $T_C = 627$ K that was not completely reacted in the initial LaNi precursor seems a likely possibility. The measured value $M_0 \sim 2.5 \times 10^{-4} \mu_B$/Ni in La$_2Ni_2$In could be explained by the presence of less than 0.04% of elemental Ni, with M_0(Ni) $\sim 0.63 \mu_B$/Ni [30]. This is far less than could be detected by XRD or most analytical methods.

We find that the temperature dependence of M_0 in Fig. 6 can be explained quantitatively by assuming the presence of nanoscale clusters, each containing a few to a few dozens of magnetic ions. If the Curie temperatures of the individual nanoclusters are distributed by a function $F(T_C)$, that is, the probability to find a ferromagnetic Ni ion in a cluster with $T_C = \theta$ is $F(\theta)$, the residual magnetization $M_0(T)$ can be calculated by a simple formula:

$$M_0(T) = m_0 \int_T^\infty F(T_C) \sqrt{1 - \frac{T^2}{T_C^2}} \, dT_C, \qquad (5)$$

where m_0 represents the average concentration of ferromagnetic Ni atoms and their average magnetic moment. We first assumed the simplest possible scenario, $F(T_C) = \theta^{-1} \exp(-T_C/\theta)$, i.e., an exponential distribution with the width θ. We can then fit all experimental data very well except for the lowest temperature (Fig. 6, green solid line, $m_0 = 1.65 \times 10^{-4} \mu_B$/Ni, $\theta = 300$ K). The deviation of the lowest temperature points from this distribution, suggests that a large number of clusters have very small Curie temperatures. Indeed, it has been suggested [31] that the critical temperature of Ni nanoclusters goes down precipitously when the cluster size becomes smaller than a few nanometers, and drops to zero with clusters of the order 1–1.5 nm. To account for this effect we have added a sharp Gaussian to the assumed distribution function, namely, $F(T_C) = \exp(-T_C/\theta) + 4.75 \exp[-(T_C/\theta')^2]$, where $\theta' = \theta/10$. The physical meaning is that approximately 30% of all ferromagnetic Ni form ultrasmall clusters of only a few nanometers in size, which have a Curie temperature of less than 30 K. This modified distribution fits the entire range perfectly, as can be seen by the red curve in Fig. 6.

The slope of the $M(H)$ isotherms involved in the extrapolation of the spontaneous moment M_0 gives the effective susceptibility χ_0, which is plotted in the inset to Fig. 5. Within the accuracy of our measurement and analysis, χ_0 approaches a temperature-independent value of $\sim 2.1 \times 10^{-4}$ emu/mol below 200 K. We take this value as an estimate of the Pauli susceptibility that would be found in the absence of any ferromagnetic contamination. Using the calculated density of states, which is 4.0 states/eV/f.u., we compute a bare Pauli susceptibility $\chi_{Pauli} = 1.3 \times 10^{-4}$ emu/mol, which when compared with the experimental value of χ_0 indicates that there is a moderate magnetic enhancement of the Pauli susceptibility in La$_2$Ni$_2$In. The measured χ_0 agrees rather well with calculations of the Stoner-renormalized spin susceptibility, which appear to be about 33 % higher than the calculated Pauli susceptibility, i.e., 1.7×10^{-4} emu/mol.
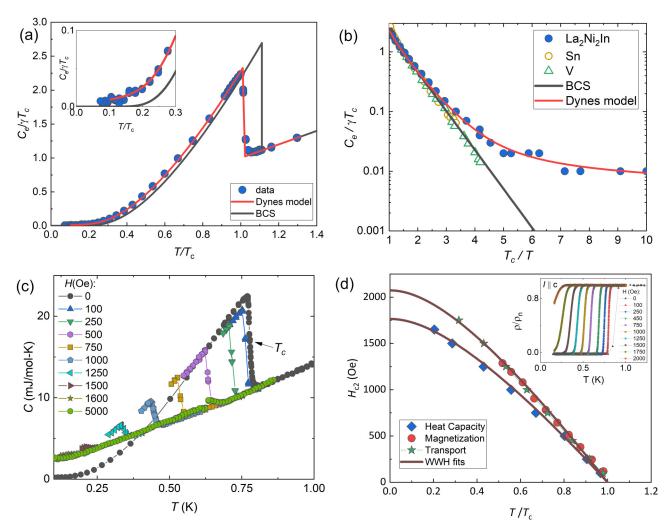
FIG. 7. Temperature dependence of the specific heat of La$_2$Ni$_2$In below 1.3 K. (a) The electronic part of the specific heat is normalized by the product of the Sommerfeld coefficient γ and the superconducting transition temperature T_c $C_e/\gamma T_c$, and is plotted as a function of T/T_c. The inset shows an enlarged view of the low-temperature region. Red line indicates fit by the Dynes model, described in the text. (b) Semilogarithmic plot of $C_e/\gamma T_c$ as a function of the normalized inverse temperature T_c/T of La$_2$Ni$_2$In as well as the two BCS superconductors Sn and V for comparison [33]. Black line is the BCS model; red line is the Dynes model. (c) The suppression of the superconducting jump at T_c in the specific heat C is measured with the magnetic field $H \perp c$. Values of the field are as indicated. (d) Derived H_{c2}-(T/T_c) phase diagram, combining values of T_c from specific heat, magnetization, and resistivity measurements. The inset shows the temperature dependencies of the electrical resistivity, measured at different fixed fields. Solid lines represent the WWH model, as discussed in the main text.

However, note that in itinerant systems, the mean-field DFT calculations tend to *over*estimate, not *under*estimate χ [32].

IV. SUPERCONDUCTING PROPERTIES

A. Specific heat

We begin our analysis of the superconductivity in La$_2$Ni$_2$In with the specific heat measurements. The contribution of the nuclear Schottky effect to the low-temperature specific heat C_{nuc} is described in Appendix D. The phonon contribution C_{ph} was determined by fitting the measured data C between 1 and 4 K to the expression $C(T) = \gamma T + \beta_1 T^3 + \beta_2 T^5$. The electronic contribution to the specific heat $C_e = C - C_{\text{nuc}} - C_{\text{ph}}$ divided by the product of the normal state Sommerfeld coefficient γ and the critical temperature T_c is plotted as a function of the normalized temperature T/T_c in Fig. 7(a). The

normal state C_e decreases linearly with T as expected for a conventional metal, until a jump in $C(T)$ at $T = T_c$ occurs that signals a second-order phase transition into the superconducting (SC) state. The transition is very narrow, as previously indicated, confirming bulk SC and a high degree of sample quality.

The magnitude of the specific heat jump $\Delta C/C_n \approx 1.21$ is about 15 % smaller than the value of 1.43 given by the BCS model in the weak-coupling limit, with C_n the normal state specific heat at the transition. In order to better understand this behavior as well as the evolution of C_e below T_c, we examined the dependence of $C_e/\gamma T_c$, plotted as a function of inverse temperature [Fig. 7(b)]. While the behavior of $C_e(T)$ in the vicinity of T_c and down to $\approx T_c/4$ is well described by the exponential function predicted by the BCS model, significant deviations are observed at lower temperatures $T < T_c/6$.

The nonexponential temperature dependence of $C_e(T)$ that is highlighted in Fig. 7(b) can be described by a sum of an exponential and a linear residual term, suggesting that $C_e(T)$ in our crystals is affected by the presence of quasiparticles with energies $E < \Delta$. This can indicate either an unconventional pairing symmetry with a nodal order parameter or subgap states in an s-wave superconductor. The subgap states at $E < \Delta$ are not accounted for in the BCS model, in which $C_e(T)$ is given by

$$C_e(T) = \frac{1}{2T^2} \int_0^\infty \left[E^2 - \frac{T}{2} \frac{\partial \Delta^2}{\partial T} \right] \frac{N(E) dE}{\cosh^2(E/2T)}. \quad (6)$$

Here $N(E) = N_0 E / \sqrt{E^2 - \Delta^2}$ at $E > \Delta$ and $N(E) = 0$ at $E < \Delta$ is the BCS density of states, and N_0 is the DOS per spin at the Fermi surface in the normal state. Because $N(E)$ vanishes at $E < \Delta$, Eq. (6) gives an exponential temperature dependence of $C_e^{BCS}(T) \sim \gamma T_c \sqrt{\Delta/T} \exp(-\Delta/T)$ at $T \ll \Delta$.

In many materials, the BCS gap singularities in $N(E)$ at $E = \Delta$ are smeared out. The resulting quasiparticle subgap states occurring at $E < \Delta$ have traditionally been addressed in the literature using the phenomenological Dynes model in which [34,35]

$$N(E) = N_0 \mathrm{Re} \frac{E - i\Gamma}{\sqrt{(E - i\Gamma)^2 - \Delta^2}}. \quad (7)$$

Here a pair-breaking parameter Γ accounts for a finite quasiparticle lifetime $\hbar/\Gamma$, resulting in a finite DOS $N(0) = N_0 \Gamma/\Delta$ at $E = 0$.

To understand the features of $C_e(T)$ observed in our crystals, we use the Dynes model in which T_c, $\Delta(T)$, and $C_e(T)$ are determined by Eqs. (E8)–(E11) given in Appendix E [36,37]. By numerically solving these equations, it is possible to fit the experimental $C_e(T)$ data, as demonstrated in Figs. 7(a) and 7(b). The Dynes model effectively captures both a nonexponential residual $C_e(T)$ at low T and the reduction of $\Delta C \approx 1.2\gamma T_c$ at $T = T_c$, substantially different from the BCS value $\Delta C = 1.43\gamma T_c$. The fit was carried out for a dimensionless pair-breaking parameter $g = \Gamma/2\pi T_{c0} = 0.02$, where Γ is taken to be independent of T. Here Γ is about seven times smaller than the critical value $\Gamma_c = \Delta_0/2$ at which T_c vanishes in the Dynes model (see Appendix E). In accordance with Fig. 7, weak pair breaking at $g = 0.02$ produces a small reduction of T_c by about 10 %, as compared to T_{c0} at $\Gamma = 0$. This suggests that T_{c0} of our crystals would be close to 0.86 K in the ideal case of $\Gamma = 0$. The overall expression of $C_e(T)$ that is calculated from Eq. (6) using the Dynes DOS with $g = 0.02$ overall agrees very well with the experimental data.

Subgap states have been revealed by numerous tunneling experiments (see, e.g., a review [35] and the references therein). Many mechanisms of subgap states have been suggested in the literature, including inelastic scattering of quasiparticles by phonons [38], Coulomb correlations [39], anisotropy of the Fermi surface [40], inhomogeneities of the BCS pairing constant [41], magnetic impurities [42], spatial correlations in impurity scattering [42,43], or diffusive surface scattering [44] (see, e.g., Ref. [45] for an overview of different mechanisms). The weak ferromagnetism associated with magnetic nanoclusters in La$_2$Ni$_2$In could potentially affect the

value of Γ in different ways. We could expect a significant contribution to Γ from spin-flip magnetic scattering, as well as the presence of localized states associated with magnetic impurities [42]. Magnetic nanoclusters can also cause local variations of the BCS pairing constant, resulting in a slight broadening of the sharp transition characteristic of the BCS and Dynes models, as well as an additional contribution to Γ [41]. Irrespective of the mechanisms, this analysis gives insight into how an underlying broadening of the DOS gap peaks can account for the behavior of $C_e(T)$ observed in our crystals. We note that $C_e(T)$ at $T \lesssim T_c/2$ is mostly determined by thermally activated quasiparticles with energies $E \approx \Delta$, but at lower temperatures $C_e(T)$ is dominated by quasiparticles with $E \sim T \ll \Delta$, leading to a residual specific heat $C_i \sim \gamma T \Gamma/\Delta$ [37].

Beyond the effects of magnetic pair breaking by dilute magnetic impurities [46,47], our fits based on the Dynes model accurately describe the jump in the specific heat ΔC at $T = T_c$ and the overall temperature dependence of $C_e(T)$ within the superconducting state, while implying that T_c is further reduced from the value determined by only magnetic pair breaking. We will consider below the possibility that this additional density of states is related to a nodal order parameter in La$_2$Ni$_2$In.

B. Magnetism and the superconducting state

Figure 8 shows representative magnetization measurements of La$_2$Ni$_2$In at temperatures ranging from 0.39 to 1.15 K. The data in Figs. 8(a) and 8(b) were corrected for demagnetization effects due to the sample shape using the expression for a rectangular cuboid in Ref. [48]. Bulk superconductivity is evident from the sharp increase of the magnetic susceptibility after zero-field cooling (zfc) as depicted in Fig. 8(a). The SC region is characterized by a SC volume fraction of 99 %, indicating virtually perfect shielding. The sample also exhibits substantial shielding even after cooling in field (fc), indicating that pinning of flux vortices is small. The corresponding value of the Meissner fraction is 55 %. Figure 8(b) shows the ac susceptibility recorded with a field amplitude of 1 Oe and a drive frequency of 1 kHz. A sharp peak is visible in the imaginary part of the susceptibility χ'', corresponding to the SC transition. The transition temperature, defined as the maximum in χ'', was determined to be $T_c = 0.79$ K. Measurements at various drive frequencies (not shown) found no frequency dependence of the ac susceptibility.

The magnetization isotherms in the temperature range 0.39–0.74 K shown in Fig. 8(c) reveal La$_2$Ni$_2$In to be a type-II superconductor, as evidenced by the linear shielding at low fields (see dashed line in the inset). Above about 10 Oe the shielding reduces as magnetic flux starts to penetrate the sample and the system enters into the vortex state. Extracting the lower critical field H_{c1} from a linear fit to the low-field magnetization results in the phase diagram shown in Fig. 8(d). Its temperature dependence is well described by the Ginzburg-Landau expression $H_{c1}(T) = H_{c1}(0)[1 - (T/T_c)^2]$, resulting in a rather small lower critical field value of $H_{c1}(0) = 11.2(1)$ Oe. However, this values does not account for demagnetization effects. The corrected value is $H_{c1}(0)/(1 - N) =$
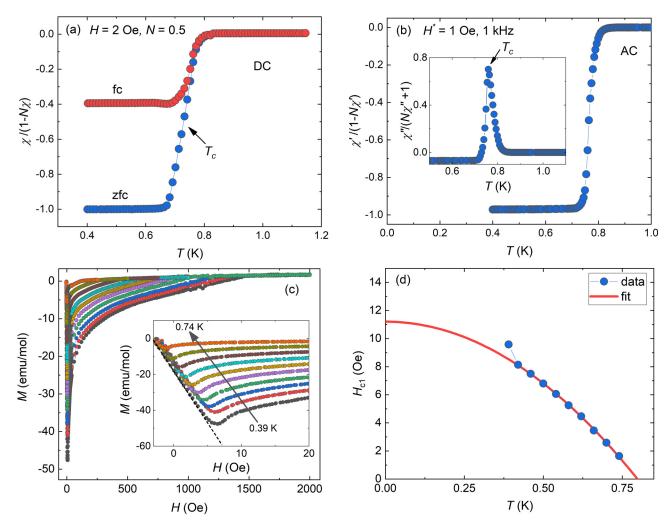
FIG. 8. Measurements of the magnetization of La$_2$Ni$_2$In in the superconducting state. (a) Temperature dependencies of the dc field-cooled (fc) and zero-field cooled (zfc) magnetic susceptibility near the superconducting transition temperature T_c. (b) Real (main figure) and imaginary (inset) parts of the ac susceptibility χ' below 1 K, with field amplitude $H^* = 1$ Oe and drive frequency 1 kHz. (c) Field dependencies of the magnetization measured at fixed temperatures ranging from 0.39 to 0.74 K. The inset shows an enlarged view of the low-field data. The black dashed line is a guide to the eye that emphasizes the linear part of $M(H)$. (d) Extracted values of the lower critical field presented as a function of temperature T (solid symbols), including a fit to a Ginzburg-Landau expression (solid line) that is described in the main text.

14.0(1) Oe, with $N = 0.2$ for the sample used in Figs. 8(c) and 8(d).

Upon application of a magnetic field the SC transition is continuously suppressed to lower temperatures, as shown in Fig. 7(c). For fields above 500 Oe, SC is fully suppressed and normal metallic behavior is recovered over the depicted temperature range. Extracting transition temperatures from the inflection points of the curves and plotting them as a function of the reduced temperature results in Fig. 7(d), where we also included data obtained from measurements of the magnetization and resistivity at various applied fields (see inset). The H_{c2} data are described well by the single-band Werthamer, Helfand, and Hohenberg (WHH) theory [49]. The fit to the data yields an average upper critical field of $H_{c2}(0) = 1918(19)$ Oe at $T = 0$. Hence, we can evaluate the Ginzburg-Landau (GL) coherence length $\xi(T) = \xi(0)(1 - T/T_c)^{-1/2}$ using the WHH relation $H_{c2}(0) = 0.69\phi_0/2\pi\xi^2(0)$, where ϕ_0 is the magnetic flux quantum. This yields $\xi(0) = 34.4(2)$ nm.

It is instructive to compare the $T = 0$ values of the GL coherence length $\xi(0)$ and the BCS coherence length $\xi_0 = 0.12\hbar v_F/k_B T_c$ at $T = 0$, to determine whether La$_2$Ni$_2$In is in the clean limit [50]. Using the calculated $v_F \approx 0.2 \times 10^8$ cm/s and $T_{c0} = 0.86$ K from the specific heat data, we get $\xi_0 \approx 245$ nm, about seven times larger than $\xi(0)$. Such a large difference between $\xi(0)$ and ξ_0 indicates that our La$_2$Ni$_2$In crystals are in the dirty limit, where the mean free path due to nonmagnetic impurities ℓ_{mfp} is much shorter than ξ_0. Indeed, an estimate of ℓ_{mfp} from the residual resistivity and the calculated plasma frequency and Fermi velocity gives $\ell_{\mathrm{mfp}} \approx 10$ nm and $\ell_{\mathrm{mfp}}/\xi_0 \simeq 0.04$. The evaluation of the GL coherence length in the dirty limit $\xi(0) = 0.855(\xi_0 \ell_{\mathrm{mfp}})^{1/2}$ [50] yields $\xi(0) \approx 42.3$ nm, about 24% larger than $\xi(0)$ extracted from the H_{c2} data. Thus, the conclusion that our samples are in the dirty limit is qualitatively consistent with our H_{c2} and transport measurements. This value should be considered to be an upper bound, since a more accurate

evaluation of $\xi(0)$ requires taking into account scattering from magnetic impurities, subgap states, and strong-coupling corrections.

Next, we analyze the lower critical field H_{c1} using the GL relation:

$$H_{c1} = \frac{\phi_0}{4\pi \lambda_L^2}\left(\ln\frac{\lambda_L}{\xi} + \frac{1}{2}\right), \tag{8}$$

where λ_L is the London penetration depth and the factor of $1/2$ accounts for the vortex cores. Evaluation of $\lambda_{L0} = \hbar c/\omega_p$ in the clean limit $\ell_{mfp} \gg \xi_0$ gives $\lambda_{L0} \approx 50$ nm for the field along the c axis. Using the more appropriate dirty limit expression, $\lambda_L = \lambda_{L0}\sqrt{1 + \xi_0/\ell_{mfp}} = 250$ nm in Eq. (8), leads to $H_{c1} \approx 13.7$ Oe, which is quite close to the experimental value of 14.0 Oe. Corrections to λ_L due to magnetic impurities and subgap states were estimated to be no more than $\approx 6\%$ (see Appendix E).

The values $\xi(0) = 34.4$ nm and $\lambda_L(0) = 250$ nm were used to obtain the GL parameter $\kappa_{GL} = \lambda_L/\xi \approx 7.3$, providing additional confirmation that La_2Ni_2In is a type-II superconductor. These estimates suggest that if a sample of La_2Ni_2In were available without impurities, it would be a type-I superconductor, since $\xi_0 = 245$ nm and $\lambda_L = 50$ nm lead to a value of $\kappa_{GL} \approx 0.2$ that is much smaller than the critical GL value $1/\sqrt{2}$. The putative transition from a type-I to a type-II superconductor induced by impurities is hardly surprising, given the large BCS coherence length $\xi_0 \approx 245$ nm, and the low T_c of La_2Ni_2In. Strictly speaking, we cannot rule out the possibility that pristine La_2Ni_2In could exhibit unconventional pairing symmetries associated with sign changes in the order parameter. However, the strong impurity scattering in our samples would effectively suppress any nodal states, were they present. For this reason, we used the model of an s-wave superconductor with subgap Dynes states in our analysis of the specific heat data.

The results for the Debye temperature $T_D = 226$ K and critical temperature $T_{c0} = 0.86$ K allow us to estimate the strength of the electron-phonon coupling from the McMillan equation [51]:

$$\lambda_{MM} = \frac{1.04 + \mu^* \ln(T_D/1.45T_{c0})}{(1 - 0.62\mu^*)\ln(T_D/1.45T_{c0}) - 1.04},$$

with the Coulomb repulsion parameter assumed to be $\mu^* = 0.13$. We get a value of $\lambda_{MM} = 0.46$, reasonably close to our previous estimates above. This indicates that La_2Ni_2In is a superconductor in the weak- to intermediate-coupling regime. The value derived above is in agreement with the mass renormalization deduced from specific heat and from λ_{tr}, which are 0.38 and 0.395, respectively. A slightly larger value of the McMillan λ_{MM} likely reflects the difference between the Debye and the logarithmic frequencies.

A summary of the various properties derived in this analysis can be found in Table II.

V. CONCLUSION

We have synthesized high-quality single crystals of La_2Ni_2In, previously only available in polycrystalline form.

Resistivity measurements show good metallic behavior, in agreement with DFT calculations. The density of states taken from the Sommerfeld coefficient of the specific heat is only slightly enhanced relative to the one determined from the DFT calculations, signaling only weak electronic correlations. Unlike the more highly studied members of the R_2T_2X ($R =$ rare earth, $T =$ transition metal, $X =$ main group element) family, DFT calculations indicate that the Ni states lie well below the Fermi energy, with a substantial degree of charge transfer that ensures that the Ni magnetism is quenched. Measurements of the magnetization reveal weak ferromagnetism that is associated with ferromagnetic contamination, most likely elemental Ni. The remainder of the magnetic susceptibility is nearly temperature independent, as expected for the Pauli susceptibility. Relative to the value of the Pauli susceptibility expected for the density of states taken from the measured Sommerfeld constant, we infer that there is a weak enhancement that is of similar magnitude to the small Stoner factor determined from the DFT calculations. Our measurements and the DFT calculations together imply that La_2Ni_2In is best understood as a good metal with minimal electronic correlations. Superconductivity is observed below 0.9 K, in good agreement with the McMillan expression for T_c, using values of the electron-phonon interaction taken from the DFT calculations. A detailed analysis of the magnetic susceptibility and specific heat in the superconducting state find that La_2Ni_2In is a type-II superconductor that is in the dirty limit, although there are indications that it could be type I in the absence of impurities. Our analysis using the phenomenological Dynes model highlights important roles for subgap quasiparticle states, beyond those expected from pair breaking alone. To the best of our knowledge, La_2Ni_2In is the first superconductor reported in this family of compounds. The weakness of the Ni magnetism, and the absence of magnetic correlations are likely to make it a conventional superconductor. Considering the spectrum of behaviors that have already been observed in f-electron bearing members of this family of compounds, which range from strong local-moment magnetism, to mixed valence, and ultimately to conventional metals with differing degrees of correlations, we place La_2Ni_2In in this last category. In this way, it should be considered as analogous to other conventional superconductors with nonmagnetic or weakly magnetic Ni. Using the Sommerfeld coefficient as a proxy for the strength of electronic correlations, we find that La_2Ni_2In with $\gamma = 13$ mJ mol^{-1} K^{-2} and $T_c = 0.89$ K is much more strongly correlated than LaNiAsO ($\gamma = 3$ mJ mol^{-1} K^{-2} and $T_c = 2.7$ K) [52], but not as correlated as La_3Ni ($\gamma = 21$ mJ mol^{-1} K^{-2} and $T_c = 2.2$ K) [53], and the most correlated La_7Ni_3 $\gamma = 44$ mJ mol^{-1} K^{-2} and $T_c = 2.4$ K) [54].
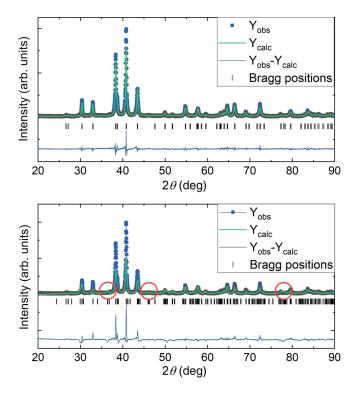
FIG. 9. Comparison between Rietveld refinements of the XRD data of La$_2$Ni$_2$In using the tetragonal model with space group $P4/mbm$ (top) and the forced orthorhombic structure with space group $Pbam$. The orthorhombic model does not fit the data as well as the tetragonal model. In particular, additional peaks are present in the orthorhombic model (circles) that are not observed in the data.

APPENDIX A: COMPARISON OF THE TETRAGONAL AND ORTHORHOMBIC STRUCTURE VARIANTS

Pustovoychenko *et al.* recently reported on the synthesis of an orthorhombic variant of La$_2$Ni$_2$In in Ref. [23]. Since our DFT calculations also seemed to favor this structure, we forced a fit with the orthorhombic $Pbam$ structure to our recorded XRD data. A direct comparison between the data fitted to the tetragonal and orthorhombic structure, respectively, can be seen in Fig. 9. Since the orthorhombic structure features peaks that are not present in our data, we conclude that we have grown the tetragonal variant.

APPENDIX B: DENSITY FUNCTIONAL CALCULATIONS OF THE PHONONS

Motivated by the deviation of the specific heat to the standard Debye model we calculated the zone-center phonon spectrum. The respective energies are listed in Table III.

APPENDIX C: SAMPLE DEPENDENCE OF THE MAGNETIC SUSCEPTIBILITY

The magnetic properties of four samples of La$_2$Ni$_2$In were measured for comparison. Sample No. 1 consisted of a coaligned stack of six single crystals, while samples No. 2–No. 4 were single crystals. All crystals were taken from the same batch and the measuring field was always applied along the c axis. Figure 10(a) depicts the temperature dependence of the dc magnetic susceptibility $\chi = M/H$ for samples No. 1 and No. 2, while Fig. 10(b) shows the temperature dependence of the spontaneous magnetization M_0 for four samples determined from the high-temperature fit to the magnetization $M(H)$ as discussed in the main text. The temperature dependencies of both χ and M_0 are similar among the samples. In the context of the ferromagnetic cluster model described in the main text, this suggests that there is little variation in the distribution of cluster sizes among the different crystals. However, the magnitudes of $\chi(T)$ vary among the crystals by approximately a factor of 2, corresponding to a factor of 2 variation in the overall amount of ferromagnetic clusters that is present in the different crystals. Overall this is a very reasonable result, considering that the origin of the ferromagnetism is most likely the inclusion of unreacted Ni from the LaNi precursor, which is common for all crystals from a single preparation batch.

Finally, Fig. 10(c) depicts the hysteresis present in La$_2$Ni$_2$In at three indicated temperatures. The magnitude of the hysteresis decreases with increasing temperture.

APPENDIX D: ISOLATING THE NUCLEAR SPECIFIC HEAT

Both La and In have large nuclear spins of $I = 7/2$ and $I = 9/2$, respectively, and thus they may generate nuclear Schottky anomalies in the low-temperature specific heat of La$_2$Ni$_2$In. In fact, our measured specific heat does exhibit
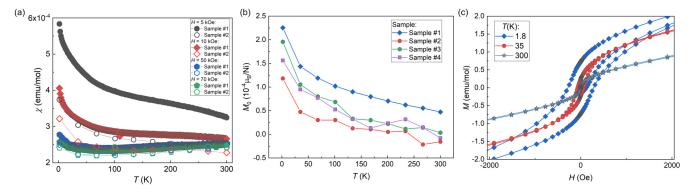

FIG. 10. Magnetic properties of various single crystals of La$_2$Ni$_2$In from the same batch. (a) Temperature dependencies of the magnetic susceptibility $\chi = M/H$ with measuring field as indicated and applied along the c axes. (b) Temperature dependencies of the spontaneous magnetization M_0 for four samples. (c) Full hysteresis loops at 1.8, 35, and 300 K measured on sample No. 1.
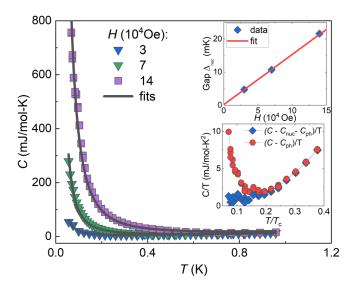
FIG. 11. Low-temperature specific heat data as a function of temperature T between 0.05 and 1 K, measured in several magnetic fields. The data were fit to the model $C(T) = C_{nuc} + C_e + C_{ph}$ defined in the main text. The upper inset shows the extracted nuclear energy gap as a function of applied magnetic field, together with a linear fit to the data (solid red line), while the lower inset shows the specific heat over temperature before and after the subtraction of the nuclear term.

a sharp increase at low temperatures in a magnetic field (Fig. 11), that gets more pronounced with increasing magnetic field. It seems likely that this contribution to the specific heat is a Schottky anomaly that is related to nuclear energy levels in either the La or the In atoms. The two-level Schottky expression is given by

$$C_{nuc}(T) = R_0 \left(\frac{\Delta_{nuc}}{T}\right)^2 \frac{\exp(\Delta_{nuc}/T)}{[1 + \exp(\Delta_{nuc}/T)]^2},$$

with energy gap Δ and R_0 the universal gas constant. At high temperatures, $T \gg \Delta$, this reduces to

$$C_{nuc}(T) \sim \frac{R_0}{4}\left(\frac{\Delta_{nuc}}{T}\right)^2 = \frac{A}{T^2}.$$

The respective least-squares fits are compared to the data in Fig. 11. The upper inset shows the field dependence of the derived energy gap Δ_{nuc}, which increases linearly from $\Delta_{nuc} = 0.17(16)$ mK at $H = 0$, signaling that the nuclear levels undergo a Zeeman splitting in the external magnetic field. Extrapolating to $H = 0$, we get a value for the coefficient of $A = 0.00(2)$ mJKmol^{-1}. Choosing $A = 1.55\,\mu$ JK/mol within the error bar, yields the corrected data that we used in our analysis. A comparison of the as-measured specific heat $C(T)$ before and after the subtraction of $C_{nuc}(T)$ is depicted in the lower inset to Fig. 11.

APPENDIX E: DYNES MODEL

Here we present the formulas of the Dynes model [36,37] used in our fits of $C_e(T)$. The equations for $\Delta(T)$ and

T_c are

$$\ln \frac{T}{T_{c0}} = 2\pi T \sum_{\omega > 0}\left[\frac{1}{\sqrt{(\omega + \Gamma)^2 + \Delta^2}} - \frac{1}{\omega}\right], \quad (E1)$$

$$\ln \frac{T_c}{T_{c0}} + \psi\left(\frac{1}{2} + \frac{\Gamma}{2\pi T_c}\right) - \psi\left(\frac{1}{2}\right) = 0, \quad (E2)$$

where $\psi(z)$ is a digamma function, ω is the Matsubara frequency, and T_{c0} is a critical temperature at $\Gamma = 0$. Equation (E2) has the same form as the Abrikosov-Gorkov equation for T_c in superconductors with magnetic impurities, so T_c decreases with Γ and vanishes at $\Gamma_c = \Delta_0/2$, where Δ_0 is the gap at $T = 0$ and $\Gamma = 0$ [42,47]. At $\Gamma \ll T_c$, Eqs. (E1) and (E2)) yield

$$T_c = T_{c0} - \frac{\pi \Gamma}{4}, \quad (E3)$$

$$\Delta \simeq \Delta_0 - \Gamma - \frac{\pi^2 \Gamma T^2}{6\Delta_0^2}, \quad T \ll T_c. \quad (E4)$$

The finite DOS at $E = 0$ in the Dynes model results in a quadratic temperature dependence of $\Delta(T)$ instead of the BCS exponential behavior of $\Delta(T) \simeq \Delta_0 - \sqrt{2\pi T \Delta_0} \exp(-\Delta_0/T)$ at $T \ll T_c$.

The magnetic penetration depth in the dirty limit is [36]

$$\frac{1}{\lambda_L^2} = \frac{\pi \mu_0 \Delta}{\hbar \rho_n} \text{Im}\psi\left(\frac{1}{2} + \frac{\Gamma}{2\pi T} + \frac{i\Delta}{2\pi T}\right), \quad (E5)$$

where ρ_n is the normal state resistivity. At $T \ll T_c$ Eq. (E5) reduces to

$$\frac{1}{\lambda_L^2} = \frac{2\mu_0 \Delta}{\hbar \rho_n} \tan^{-1} \frac{\Delta}{\Gamma}. \quad (E6)$$

The specific heat $C_e = -T \partial^2 F/\partial T^2$ is calculated using the free energy F in the Dynes model in which F is obtained by substituting $\omega \to \omega + \Gamma$ into the BCS formula for F. The result can be written in the form

$$F = F_n + 4\pi T N_0 \Delta^2 \sum_{\omega > 0}\left[\frac{1}{2\sqrt{(\omega + \Gamma)^2 + \Delta^2}} - \frac{1}{\omega + \Gamma + \sqrt{(\omega + \Gamma)^2 + \Delta^2}}\right], \quad (E7)$$

where $F_n = -\pi^2 N_0 T^2/3$ is the free energy of the normal state and N_0 is the density of states per spin.

It is convenient to recast Eqs. (E1), (E2), and (E7) in the dimensionless form

$$\ln t_c + \psi\left(\frac{1}{2} + \frac{g}{t_c}\right) - \psi\left(\frac{1}{2}\right) = 0, \quad (E8)$$

$$\ln t = \sum_{n=0}^{\infty}\left[\frac{1}{\sqrt{(n + 1/2 + g/t)^2 + s/t^2}} - \frac{1}{n + 1/2}\right], \quad (E9)$$

where $t = T/T_{c0}$, $t_c = T_c/T_{c0}$, $g = \Gamma/2\pi T_{c0}$, and $s = (\Delta/2\pi T_{c0})^2$. The normalized specific heat $c = C_e(T)/C_n(T_{c0})$, where $C_n(T_{c0}) = 2\pi^2 N_0 T_{c0}/3$, is then

$$c(t) = t - t \frac{\partial^2 f_s}{\partial t^2}, \quad (E10)$$

$$f_s = 6s \sum_{n=0}^{\infty} \left[\frac{1}{\sqrt{(n+1/2+g/t)^2 + s/t^2}} \right.$$
$$\left. - \frac{2}{n+1/2+g/t + \sqrt{(n+1/2+g/t)^2 + s/t^2}} \right].$$
$$\text{(E11)}$$

Equations (E8)–(E11) were solved numerically to fit the experimental data shown in Fig. 7. The fit was done with $g = \Gamma/2\pi T_{c0} = 0.02$ and Γ independent of T. Here $g = 0.02$ corresponds to $\Gamma/\Delta_0 = 2\pi g/1.76 = 0.07$ about seven times smaller than $\Gamma_c = \Delta_0/2$ at which $T_c \to 0$. At $g = 0.02$ weak pair breaking results in a small increase of $\lambda_L \approx 1.06\lambda_{L0}$ given by Eq. (E6).

[1] U. C. Rodewald, B. Chevalier, and R. Pöttgen, J. Solid State Chem. **180**, 1720 (2007).

[2] Y. Kalychak, V. Zaremba, R. Pöttgen, M. Lukachuk, and R.-D. Hoffmann, *Handbook on the Physics and Chemistry of Rare Earths*, edited by K. A. Gschneidner, Jr., J.-C. G. Bunzli, and V. K. Pecharsky (Elsevier, New York, 2004), Vol. 34.

[3] M. Lukachuk and R. Pöttgen, Z. Kristallogr. **218**, 767 (2003).

[4] R. Kraft and R. Pöttgen, Monatsh. Chem. **135**, 1327 (2004).

[5] M. S. Kim and M. C. Aronson, J. Phys.: Condens. Matter **23**, 164204 (2011).

[6] L. S. Wu, W. J. Gannon, I. A. Zaliznyak, A. M. Tsvelik, M. Brockmann, J.-S. Caux, M. S. Kim, Y. Qiu, J. R. D. Copley, G. Ehlers *et al.*, Science **352**, 1206 (2016).

[7] W. J. Gannon, I. A. Zaliznyak, L. S. Wu, A. E. Feiguin, A. M. Tsvelik, F. Demmel, Y. Qiu, J. R. D. Copley, M. S. Kim, and M. C. Aronson, Nat. Commun. **10**, 1123 (2019)

[8] R. Gordon, Y. Ijiri, C. Spencer, and F. DiSalvo, J. Alloys Compd. **224**, 101 (1995).

[9] J. G. Sereni, M. Gómez Berisso, G. Schmerber, and J. P. Kappler, Phys. Rev. B **81**, 184429 (2010).

[10] W. J. Gannon, K. Chen, M. Sundermann, F. Strigari, Y. Utsumi, K.-D. Tsuei, J.-P. Rueff, P. Bencok, A. Tanaka, A. Severing, and M. C. Aronson, Phys. Rev. B **98**, 075101 (2018).

[11] D. Kaczorowski, P. Rogl, and K. Hiebl, Phys. Rev. B **54**, 9891 (1996).

[12] M. Giovannini, H. Michor, E. Bauer, G. Hilscher, P. Rogl, and R. Ferro, J. Alloys Compd. **280**, 26 (1998).

[13] S. Dhar, R. Settai, Y. Ōnuki, A. Galatanu, Y. Haga, P. Manfrinetti, and M. Pani, J. Magn. Magn. Mater. **308**, 143 (2007).

[14] R. Hauser, H. Michor, E. Bauer, G. Hilscher, and D. Kaczorowski, Phys. B: Condens. Matter **230–232**, 211 (1997).

[15] L. Havela, V. Sechovský, P. Svoboda, M. Diviš, H. Nakotte, K. Prokeš, F. R. de Boer, A. Purwanto, R. A. Robinson, A. Seret *et al.*, J. Appl. Phys. **76**, 6214 (1994).

[16] T. Muramatsu, T. Kanemasa, T. Kagayama, K. Shimizu, Y. Aoki, H. Sato, M. Giovannini, P. Bonville, V. Zlatic, I. Aviani *et al.*, Phys. Rev. B **83**, 180404(R) (2011).

[17] G. Lamura, I. J. Onuorah, P. Bonfà, S. Sanna, Z. Shermadini, R. Khasanov, J.-C. Orain, C. Baines, F. Gastaldo, M. Giovannini *et al.*, Phys. Rev. B **101**, 054410 (2020).

[18] E. Bauer, G. Hilscher, H. Michor, C. Paul, Y. Aoki, H. Sato, D. T. Adroja, J.-G. Park, P. Bonville, C. Godart *et al.*, J. Phys.: Condens. Matter **17**, S999 (2005).

[19] P. Blaha, K. Schwarz, G. Madsen, D. Kvasnicka, and J. Luitz, *WIEN2k, An Augmented Plane Wave + Local Orbitals Program for Calculating Crystal Properties* (Techn. Universität Wien, Wien, 2001).

[20] G. Kresse and J. Furthmüller, Phys. Rev. B **54**, 11169 (1996).

[21] J. P. Perdew, K. Burke, and M. Ernzerhof, Phys. Rev. Lett. **77**, 3865 (1996).

[22] Y. M. Kalychak, V. I. Zaremba, V. M. Baranyak, P. Y. Zavalii, V. A. Bruskov, L. V. Sysa, and O. V. Dmytrakh, Inorg. Mater. (Engl. Transl.) **26**, 74 (1990).

[23] M. Pustovoychenko, V. Svitlyk, and Y. Kalychak, Intermetallics **24**, 30 (2012).

[24] M. Milewits, S. J. Williamson, and H. Taub, Phys. Rev. B **13**, 5199 (1976).

[25] D. W. Woodard and G. D. Cody, Phys. Rev. **136**, A166 (1964).

[26] J. C. H. Chiu, Phys. Rev. B **13**, 1507 (1976).

[27] J. Ziman, *Electrons and Phonons* (Oxford University Press, New York, 1960).

[28] B. Chakraborty, W. E. Pickett, and P. B. Allen, Phys. Rev. B **14**, 3227 (1976).

[29] A. Arrott, Phys. Rev. **108**, 1394 (1957).

[30] B. Chiffey and T. Hicks, Phys. Lett. A **34**, 267 (1971).

[31] X. He, W. Zhong, C.-T. Au, and Y. Du, Nanoscale Res. Lett. **8**, 446 (2013).

[32] T. Moriya, *Spin Fluctuations in Itinerant Electron Magnetism*, Springer Series in Solid-State Sciences (Springer, Berlin/Heidelberg, 2012).

[33] S. Hunklinger, *Festkörperphysik* (De Gruyter Oldenbourg, Munich, 2018).

[34] R. C. Dynes, V. Narayanamurti, and J. P. Garno, Phys. Rev. Lett. **41**, 1509 (1978).

[35] J. Zasadzinski, Tunneling spectroscopy of conventional and unconventional superconductors, in *The Physics of Superconductors*, edited by K. H. Bennemann and J. B. Ketterson (Springer, New York, 2003), Chap. 15, p. 591.

[36] A. Gurevich and T. Kubo, Phys. Rev. B **96**, 184515 (2017).

[37] F. Herman and R. Hlubina, Phys. Rev. B **96**, 014509 (2017); **97**, 014517 (2018).

[38] T. P. Devereaux and D. Belitz, Phys. Rev. B **44**, 4587 (1991).

[39] D. A. Browne, K. Levin, and K. A. Muttalib, Phys. Rev. Lett. **58**, 156 (1987).

[40] A. J. Bennett, Phys. Rev. **140**, A1902 (1965).

[41] A. l. Larkin and Y. N. Ovchinnikov, J. Exp. Theor. Phys. **34**, 1144 (1972).

[42] A. V. Balatsky, I. Vekhter, and J. X. Zhu, Rev. Mod. Phys. **78**, 373 (2006).

[43] J. S. Meyer and B. D. Simons, Phys. Rev. B **64**, 134516 (2001).

[44] E. Wolf and G. Arnold, Phys. Rep. **91**, 31 (1982).

[45] M. A. Skvortsov and M. V. Feigel'man, J. Exp. Theor. Phys. **117**, 487 (2013).

[46] L. A. Openov, Phys. Rev. B **69**, 224516 (2004).

[47] K. Maki, in *Superconductivity*, edited by R. D. Parks (Marcel Dekker, Inc., New York, 1969), Vol. 2, p. 1035.

[48] R. Prozorov and V. G. Kogan, Phys. Rev. Appl. **10**, 014030 (2018).

[49] N. R. Werthamer, E. Helfand, and P. C. Hohenberg, Phys. Rev. **147**, 295 (1966).

[50] M. Tinkham, *Introduction to Superconductivity* (Dover, Mineola, NY, 2004).

[51] W. L. McMillan, Phys. Rev. **167**, 331 (1968).

[52] Y. Li, Y. Luo, L. Li, B. Chen, X. Xu, J. Dai, X. Yang, L. Zhang, G. Cao, and Z.-a. Xu, J. Phys.: Condens. Matter **26**, 425701 (2014).

[53] N. Sato, K. Imamura, T. Sakon, T. Komatsubara, I. Umehara, and K. Sato, J. Phys. Soc. Jpn. **63**, 2061 (1994).

[54] A. Nakamura, F. Honda, Y. Homma, D. Li, K. Nishimura, M. Kakihana, M. Hedo, T. Nakama, Y. Ōnuki, and D. Aoki, J. Phys.: Conf. Ser. **807**, 052012 (2017).